3212 *Chem. Mater.* **2010,** *22,* 3212–3225
DOI:10.1021/cm100458b

CHEMISTRY OF MATERIALS
Article

Nucleation Control of Size and Dispersity in Aggregative Nanoparticle Growth. A Study of the Coarsening Kinetics of Thiolate-Capped Gold Nanocrystals

Shawn P. Shields, Vernal N. Richards, and William E. Buhro*

Department of Chemistry and Center for Materials Innovation, Washington University, St. Louis, Missouri 63130-4899

Received February 12, 2010. Revised Manuscript Received April 1, 2010

The thermal coarsening (180 °C) of decanethiolate-capped Au nanocrystals is studied at various tetraoctylammonium bromide concentrations. The coarsening kinetics are determined by measuring nanocrystal size distributions (CSDs) as a function of time. The results are shown to be consistent with aggregative nucleation and growth. For each kinetic trial, the time dependence of the aggregative nucleation rate is extracted from the early time CSDs and fitted by a Gaussian profile. The height of the profile is the maximum nucleation rate, Γ_{max}, and the 2σ width is the time window for nucleation, Δt_n. These nucleation parameters are shown to control the final mean size and size distribution of the coarsened nanocrystals. The coarsening kinetics are influenced by tetraoctylammonium bromide concentration because the nanocrystals are partially electrostatically stabilized.

Introduction

Here we show the kinetics of thermal coarsening of decanethiolate-capped Au nanocrystals[1,2] to be consistent with aggregative growth, wherein small, primary nanocrystals aggregate and coalesce to produce larger nanocrystals. We have analyzed the growth kinetics by adapting a classical nucleation-and-growth model to aggregative processes. Most significantly, we have experimentally measured the nucleation function, the time dependence of the aggregative-nucleation rate, which ultimately determines the final size and size distribution of the nanocrystals. The experimental nucleation function affords the maximum aggregative-nucleation rate and the width of the time window for nucleation. These *nucleation* parameters may be usefully compared to aggregative-*growth* rates extracted from a KJMA phase-transformation model. The results confirm that thiolate-capped Au nanocrystals prepared by the Brust synthesis[3] are at least partially electrostatically stabilized.[4]

Two of the most important issues confronting nanocrystal synthesis are obtaining purposeful control over the nanocrystal mean size and routinely producing narrow size distributions. General means for achieving these goals have not yet emerged, because the mechanisms of nanocrystal growth are currently poorly understood in the synthetic community.

The LaMer mechanism[5−7] is most commonly invoked,[8−13] which was originally developed to account for the growth of near-monodisperse, micrometer-scale sulfur sols in aqueous dispersion. This mechanism posits a narrow, early time window for particle nucleation, which establishes the number of nuclei viable for growth. After the nucleation period, the nuclei then grow into particles by molecular addition of nutrient species to their surfaces. Because all the particles are nucleated in a narrow time interval, and grow competitively by near-equal division of the available nutrient, they are all nearly the same size, or near monodisperse, at the end of the growth period. We shall refer to this process as classical nucleation and growth. In principle, a knowledge of the number of nuclei formed in the nucleation window and the amount of nutrient available would allow prediction of the final particle mean size. Therefore, if nanocrystals are grown by the LaMer mechanism, purposeful control over mean size and size distribution would require control over the classical nucleation process.

However, several studies have established that many and perhaps most solution-based syntheses of near-monodisperse

*To whom correspondence should be addressed. E-mail: buhro@wustl.edu.

(1) Maye, M. M.; Zheng, W.; Leibowitz, F. L.; Ly, N. K.; Zhong, C.-J. *Langmuir* **2000**, *16*, 490–497.
(2) Maye, M. M.; Zhong, C.-J. *J. Mater. Chem.* **2000**, *10*, 1895–1901.
(3) Brust, M.; Walker, M.; Bethell, D.; Schiffrin, D. J.; Wyman, R. *J. Chem. Soc., Chem. Commun.* **1994**, 801–802.
(4) Waters, C. A.; Mills, A. J.; Johnson, K. A.; Schiffrin, D. J. *J. Chem. Soc., Chem. Commun.* **2003**, 540–541.
(5) LaMer, V. K.; Dinegar, R. H. *J. Am. Chem. Soc.* **1950**, *72*, 4847–4854.
(6) LaMer, V. K. *Ind. Eng. Chem.* **1952**, *44*, 1270–1277.
(7) Reiss, H. *J. Chem. Phys.* **1951**, *19*, 482–487.
(8) Morales, M. P.; González-Carreño, T.; Serna, C. J. *J. Mater. Res.* **1992**, *7*, 2538–2545.
(9) Murray, C. B.; Norris, D. J.; Bawendi, M. G. *J. Am. Chem. Soc.* **1993**, *115*, 8706–8715.
(10) Saunders, A. E.; Sigman, M. B.; Korgel, B. A. *J. Phys. Chem. B* **2004**, *108*, 193–199.
(11) Drofenik, M.; Kristl, M.; Žnidaršič, A.; Hanžel, D.; Lisjak, D. *J. Am. Ceram. Soc.* **2007**, *90*, 2057–2061.
(12) Robb, D. T.; Privman, V. *Langmuir* **2008**, *24*, 26–35.
(13) Zheng, H.; Smith, R. K.; Jun, Y.-w.; Kisielowski, C.; Dahmen, U.; Alivisatos, A. P. *Science* **2009**, *324*, 1309–1312.

Published on Web 04/15/2010

nano- and microparticles do not conform to the LaMer mechanism.[14−35] The principal deficiency is that the LaMer mechanism does not account for the aggregation of small nanocrystallites, which has been shown to participate in the growth processes in many cases. Evidence for aggregative growth includes direct observation of particles composed of smaller primary nanocrystals,[20,22,28,32−35] decreasing particle number densities with time,[25,26,30,36] kinetic studies,[15−19] and the time evolution of (nano)crystal size distributions (CSDs).[22−26,30,31] Additionally, theoretical results establish that small nanocrystals are colloidally unstable and aggregate on time scales faster than classical growth.[30] Furthermore, Alivisatos and co-workers recently reported videos of aggregative growth recorded in TEM studies.[13] Indeed, a reexamination of the growth of LaMer sulfur sols established that the particle number density goes through a maximum after the nucleation period has ended,[36] strongly implicating the participation of aggregative processes even in this archetypal case.[36−38]

Aggregative nanocrystal growth is now becoming well recognized in the mechanistic community. The contributions of Alivisatos,[13] Banfield,[33−35] Finke,[15−19] Matijević,[20−23] Penn,[27,32−34] Privman,[22−24] Tsapatsis,[26,27] Turkevich,[28] and Zukoski[29−31] are cited above. Additionally, colloidal crystallization, which is inherently an aggregative process, is now commonly used in the mechanistic community as a model for classical nucleation and growth.[39−41] However, apart from oriented attachment,[32−35] the synthetic community is largely unaware of nanocrystal aggregation as a potentially useful mechanism for nanoparticle growth. We will argue herein that aggregative growth has intrinsic advantages for achieving dispersity and diameter control in nanocrystal syntheses.

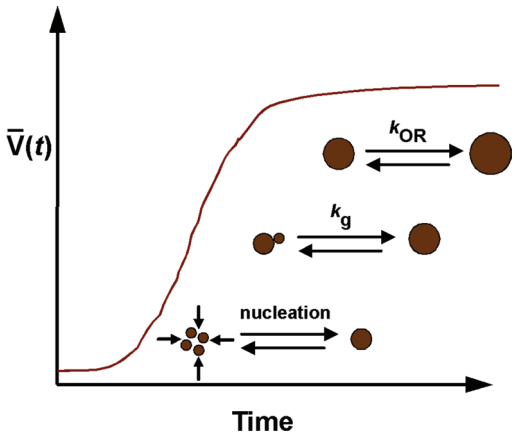

Figure 1. Schematic diagram of three stages of nanocrystal growth, nucleation, growth, and Ostwald ripening, and the commonly observed sigmoidal kinetic profile. $\bar{V}(t)$ is the mean nanocrystal volume at time t. The nucleation and growth steps depicted may refer to either the classical or aggregative mechanism. In the former case, the smallest circles represent atoms or ions, and in the latter case small, primary nanocrystals.

When aggregative processes dominate nanoparticle growth, by definition the classical nucleation and growth that precede aggregation are rapid and not rate determining. The number of viable, growing particles is established during the assembly of critical-sized *aggregates* of smaller, or primary, nanocrystallites (see Figure 1).[21,23,24,29,30] This process may be considered a second nucleation step, a *nonclassical*, aggregative nucleation step.[21,23−25,29,42] The critical aggregates so assembled may remain as aggregates,[20,22,28] or coalesce to single or polycrystalline particles.[2,17,27,28,32−35,43,44] Growth is subsequently accomplished by addition of primary nanocrystallites to the critical aggregates,[21−24,29,30] and then to the resulting supercritical nanoparticles, until all primary nanocrystallites are consumed and active growth ceases (see Figure 1). We show here that control over nanoparticle growth in such cases may be achieved by controlling the nonclassical, aggregative-nucleation process.

The classical, LaMer model for nucleation in a closed system (that is, having a fixed amount of precursor) features an initially increasing nucleation rate as nutrient concentration increases and critical nuclei are assembled, which rises to a maximum and subsequently falls off as supersaturation and therefore the driving force for nucleation is relieved.[5−7] We will refer to this time-dependent nucleation rate as the nucleation function. In the absence of aggregation, the width of the classical nucleation function, or the time window for nucleation, determines

(14) Calvert, P. *Nature* **1994**, *367*, 119–120.
(15) Hornstein, B. J.; Finke, R. G. *Chem. Mater.* **2004**, *16*, 139–150.
(16) Besson, C.; Finney, E. E.; Finke, R. G. *J. Am. Chem. Soc.* **2005**, *127*, 8179–8184.
(17) Besson, C.; Finney, E. E.; Finke, R. G. *Chem. Mater.* **2005**, *17*, 4925–4938.
(18) Finney, E. E.; Finke, R. G. *Chem. Mater.* **2008**, *20*, 1956–1970.
(19) Ott, L. S.; Finke, R. G. *Chem. Mater.* **2008**, *20*, 2592–2601.
(20) Matijević, E. *Chem. Mater.* **1993**, *5*, 412–426.
(21) Matijević, E.; Goia, D. *Croatica Chem. Acta* **2007**, *80*, 485–491.
(22) Privman, V.; Goia, D. V.; Park, J.; Matijević, E. *J. Colloid Interface Sci.* **1999**, *213*, 36–45.
(23) Libert, S.; Gorshkov, V.; Goia, D.; Matijević, E.; Privman, V. *Langmuir* **2003**, *19*, 10679–10683.
(24) Privman, V. *Ann. N.Y. Acad. Sci.* **2009**, *1161*, 508–525.
(25) Drews, T. O.; Katsoulakis, M. A.; Tsapatsis, M. *J. Phys. Chem. B* **2005**, *109*, 23879–23887.
(26) Drews, T. O.; Tsapatsis, M. *Microporous Mesoporous Mater.* **2007**, *101*, 97–107.
(27) Kumar, S.; Davis, T. M.; Ramanan, H.; Penn, R. L.; Tsapatsis, M. *J. Phys. Chem. B* **2007**, *111*, 3398–3403.
(28) Turkevich, J. *Gold Bull.* **1985**, *18*, 86–91.
(29) Look, J.-L.; Bogush, G. H.; Zukoski, C. F. *Faraday Discuss. Chem. Soc.* **1990**, *90*, 345–357.
(30) Bogush, G. H.; Zukoski, C. F. *J. Colloid Interface Sci.* **1991**, *142*, 19–34.
(31) Van Hyning, D. L.; Klemperer, W. G.; Zukoski, C. F. *Langmuir* **2001**, *17*, 3128–3135.
(32) Penn, R. L. *J. Phys. Chem. B* **2004**, *108*, 12707–12712.
(33) Penn, R. L.; Banfield, J. F. *Science* **1998**, *281*, 969–971.
(34) Penn, R. L.; Banfield, J. F. *Geochim. Cosmochim. Acta* **1999**, *63*, 1549–1557.
(35) Huang, F.; Zhang, H.; Banfield, J. F. *Nano Lett.* **2003**, *3*, 373–378.
(36) Levit, A. B.; Rowell, R. L. *J. Colloid Interface Sci.* **1975**, *50*, 162–169.
(37) Kerker, M.; Daby, E.; Cohen, G. L.; Kratohvil, J. P.; Matijević, E. *J. Phys. Chem.* **1963**, *67*, 2105–2111.
(38) Rowell, R. L.; Kratohvil, J. P.; Kerker, M. *J. Colloid Interface Sci.* **1968**, *27*, 501–506.
(39) Gasser, U.; Weeks, E. R.; Schofield, A.; Pusey, P. N.; Weitz, D. A. *Science* **2001**, *292*, 258–262.
(40) Gong, T.; Shen, J.; Hu, Z.; Marquez, M.; Cheng, Z. *Langmuir* **2007**, *23*, 2929–2923.
(41) Dixit, N. M.; Zukoski, C. F. *Phys. Rev. E* **2002**, *66*, 125602.
(42) Prakash, A.; Bapat, A. P.; Zachariah, M. R. *Aerosol Sci. Technol.* **2003**, *37*, 892–898.
(43) Uyeda, N.; Nishino, M.; Suito, E. *J. Colloid Interface Sci.* **1973**, *43*, 264–275.
(44) Bisson, L.; Boissiere, C.; Nicole, L.; Grosso, D.; Jolivet, J. P.; Thomazeau, C.; Uzio, D.; Berhault, G.; Sanchez, C. *Chem. Mater.* **2009**, *21*, 2668–2678.

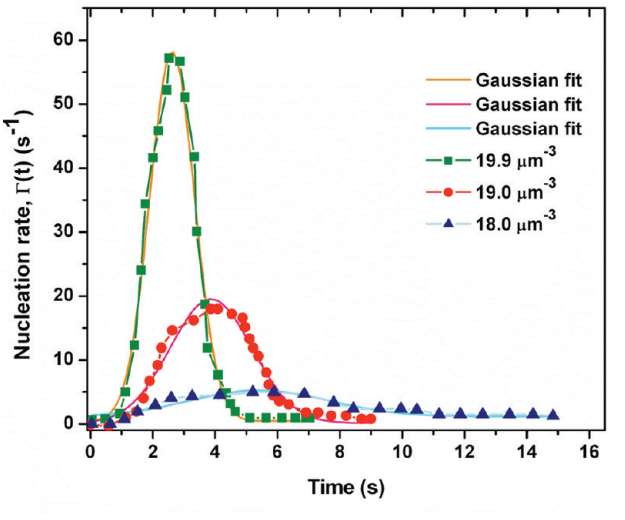

Figure 2. Nucleation functions reported by Wette and co-workers[46] for the crystallization of charged colloidal polymer spheres at three particle number densities listed in the inset legend. Gaussian fits to the nucleation-rate data are also plotted. Adapted with permission from Wette, P.; Schöpe, H. J.; Palberg, T. *J. Chem. Phys.* **2005**, *123*, 174902. Copyright 2005, American Institute of Physics.

the final size distribution. In the absence of aggregation, the integrated area under the classical nucleation function determines the number of growing particles, and therefore, along with the quantity of nutrient present, determines the final average particle size. We will show here, as others have shown previously, that the nucleation function for nonclassical, aggregative nucleation exhibits the same general features (see Figure 2).[45,46]

The very short spatial and time scales have precluded direct observation of a classical nucleation process. However, the longer spatial and time scales associated with colloidal[39] and protein[47] crystallization have recently allowed the sizes of critical aggregates (aggregative nuclei) to be directly measured. Indeed, it is the increased length and time scales that make colloidal crystallization a good model for classical nucleation and growth.[39−41]

Complete nucleation functions have been experimentally determined in a few such cases.[45,46] Figure 2 replots experimental nucleation functions for the colloidal crystallization of charged copolymer spheres reported by Wette and co-workers.[46] These nucleation functions were constructed from video data collected from an optical microscope. The reader will note that the aggregative nucleation rate rises to a maximum and then falls off in time in a manner analogous to that predicted by the classical LaMer model (see above).

Similarly, the comparatively large dimensions (1.68 ± 0.36 nm) of the primary Au nanocrystallites studied here allow us to experimentally measure the critical aggregate size and to obtain the aggregative-nucleation function from the early time CSDs collected in coarsening experiments. The maximum aggregative-nucleation rate and the width of the time window for aggregative nucleation are extracted from the aggregative-nucleation function. We will argue that these nucleation parameters are the important control factors for aggregative-nanoparticle growth.

The coarsening of decanethiolate-capped Au nanocrystals in the presence of tetra-*n*-octylammonium bromide (*n*-octyl$_4$NBr, TOABr) originally reported by Zhong and co-workers[1,2] motivated this study. The coarsening kinetics were studied here as a function of the TOABr concentration. The time window for aggregative nucleation was found to vary smoothly with TOABr concentration, and to correlate with the final nanoparticle size and size distribution. The results confirm that aggregative growth may in this case be electrostatically manipulated, and establish the synthetic utility of achieving control over the aggregative-nucleation process.

The growth rates were subsequently extracted from a KJMA model that fit the kinetic (nanoparticle mean size vs time) data well. An alternative analytical model to fit the kinetic data, based on a Finke-type mechanism, will be reported later.[47]

The thermal coarsening (or ripening) of Au and other noble-metal nanocrystals has previously been well studied for its synthetic potential, and here, we cite examples from the work of Klabunde,[48,49] Peng,[50−52] Stucky,[53] and their co-workers. Such processes may be ascribed to Ostwald ripening[54,55] or inverse Ostwald ripening (digestive ripening),[56] which is the operative mechanism under appropriate conditions. Indeed, we did observe Ostwald ripening at the end of our coarsening experiments, after the active, rapid growth periods and after the conclusion of our kinetics trials.

However, we provide evidence that excludes Ostwald ripening as the primary growth mechanism during the active growth period, including the observation of polycrystalline particles and early time bimodal size distributions, which are inconsistent with Ostwald ripening. The sigmoidal growth kinetics observed are also inconsistent with equilibrium Ostwald ripening.[57,58] Finally, close correlation of the extracted nucleation parameters with the final mean sizes and size distributions also argue against Ostwald ripening as the primary growth mechanism. The results reported here underscore the importance of considering aggregative growth as a viable mechanism,

(45) Ben-Eliyahu, Y.; Brill, M.; Mintz, M. H. *J. Chem. Phys.* **1999**, *111*, 6053–6060.
(46) Wette, P.; Schöpe, H. J.; Palberg, T. *J. Chem. Phys.* **2005**, *123*, 174902.
(47) Shields, S. P.; Buhro, W. E.; Finney, E. E.; Finke, R. G. manuscript in preparation.
(48) Lin, X. M.; Sorensen, C. M.; Klabunde, K. J. *J. Nanoparticle Res.* **2000**, *2*, 157–164.
(49) Stoeva, S.; Klabunde, K. J.; Sorensen, C. M.; Dragieva, I. *J. Am. Chem. Soc.* **2002**, *124*, 2305–2311.
(50) Jana, N. R.; Peng, X. *J. Am. Chem. Soc.* **2003**, *125*, 14280–14281.
(51) Ji, X.; Song, X.; Li, J.; Bai, Y.; Yang, W.; Peng, X. *J. Am. Chem. Soc.* **2007**, *129*, 13939–13948.
(52) Zhao, L.; Ji, X.; Li, J.; Yang, W.; Peng, X. *J. Phys. Chem. C* **2009**, *113*, 16645–16651.
(53) Zheng, N.; Fan, J.; Stucky, G. D. *J. Am. Chem. Soc.* **2006**, *128*, 6550–6551.
(54) Luo, G. *Mater. Lett.* **2007**, *61*, 1039–1041.
(55) Meli, L.; Green, P. F. *ACS Nano* **2008**, *2*, 1305–1312.
(56) Lee, D.-K.; Park, S.-I.; Lee, J. K.; Hwang, N.-M. *Acta Mater.* **2007**, *55*, 5281–5288.
(57) Seshadri, R.; Subbanna, G. N.; Vijayakrishnan, V.; Kulkarni, G. U.; Ananthakrishna, G.; Rao, C. N. R. *J. Phys. Chem.* **1995**, *99*, 5639–5644.
(58) Biswas, K.; Varghese, N.; Rao, C. N. R. *Small* **2008**, *4*, 649–655.

in addition to Ostwald ripening, for the coarsening of small nanocrystals.

The primary contribution of this study is the first quantitative experimental method for determining the nucleation function, the time width and maximum rate of nucleation, for the aggregative growth of nanocrystals. Significantly, the nucleation parameters are demonstrated to correlate strongly with the nanocrystal final mean size and size distribution. This approach may lead to powerful new methods for rational size control in nanocrystal synthesis. A table of abbreviations used is provided as Supporting Information (Table S1).

Experimental Section

General Methods and Materials. Decanethiol, tetraoctylammonium bromide (TOABr), hydrogen tetrachloroaurate (III) trihydrate ($HAuCl_4 \cdot 3H_2O$), sodium borohydride ($NaBH_4$), toluene, ethanol (EtOH), and diphenylmethane were purchased from Aldrich and used as received. All preparations and coarsening (growth) experiments were conducted under an ambient atmosphere. The coarsening experiments were conducted in a 300 mL oil bath controlled by an Ace Glass Temperature Controller with a Pt thermocouple. TEM grids were obtained from Ted Pella. Carbon Type-B, 300-mesh copper grids were used with the carbon support intact. Digital TEM images were obtained using a JEOL 2000 FX instrument operating at 200 kV and fitted with a Gatan camera.

Preparation of the Primary Decanethiol-Capped Au Nanocrystals. The primary Au nanocrystals used in the thermal coarsening experiments were synthesized using the standard two-phase method,[3] which is briefly summarized here to incorporate our modifications. Under vigorous stirring, an aqueous solution of $HAuCl_4 \cdot 3H_2O$ (0.011 M, 50 mL, 0.55 mmol) was combined with a toluene solution of TOABr (0.036 M, 50 mL, 1.8 mmol), resulting in a deep-orange mixture. After the mixture was stirred for 5 min, a toluene solution of decanethiol (0.13 M, 10 mL, 1.3 mmol) was added, producing an opaque white mixture. Subsequently, an aqueous solution (10 mL) of $NaBH_4$ (30 mg, 0.8 mmol) was added rapidly, quickly turning the mixture to a dark brown as the Au nanocrystals formed. The reaction mixture was stirred an additional 4 h and then allowed to stand ($\leq$10 min), whereupon the aqueous and toluene phases separated. The aqueous phase was discarded, and the volume of the toluene phase was reduced to $\sim$5 mL by rotary evaporation. Immediately thereafter, EtOH (200 mL) was added to the toluene dispersion, and the mixture was swirled for several minutes to precipitate the Au nanocrystals. The mixture was then allowed to stand (2−4 h), and the nanoparticles were separated by centrifugation (benchtop centrifuge). The EtOH was then decanted. The nanocrystals were redispersed in hexane (15 mL) to facilitate transfer, and dried in vacuo. (For the coarsening experiments described below, the hexane dispersion was divided into two equal aliquots, which were dried separately. Thus each coarsening experiment used half the total yield of this synthesis.) The total mass yield of decanethiol-capped Au nanocrystals was 160 mg. A simple statistical analysis of TEM images of the nanocrystals established a mean nanocrystal diameter of 1.68 nm with a standard deviation of 0.36 nm. However, the size distribution was found to be log-normal, as shown in Supporting Information Figure S1.

Conditions for Measuring the Coarsening Kinetics of Decanethiolate-Capped Au Nanocrystals. Newly synthesized nanoclusters (half of the above yield or 80 mg) were redispersed in 5.00 mL of diphenylmethane and placed in a 50 mL round-bottom Schlenk flask. Decanethiol (0.70 mL) was measured with a graduated pipet and added to the flask with swirling. The desired amount of TOABr was weighed to two decimal places and added to the nanoparticle solution. The resulting TOABr concentrations were calculated from the total volume of the mixtures (see the Supporting Information Figure S2). The concentrations (masses) of TOABr used were 0.145 M (0.50 g), 0.264 M (1.00 g), 0.362 M (1.50 g), 0.446 M (2.00 g), 0.579 M (3.00 g), 0.634 M (3.50 g), and 0.681 M (4.00 g). The flask was capped and shaken thoroughly to mix the contents, resulting in a thick, dark brown coating on the walls of the flask. TEM analysis prior to heating indicated that the nanoparticle dispersions were stable to aggregation at all TOABr concentrations used.

The flask was placed in a thermostatically controlled oil bath preheated to 180 $\pm$ 0.1 °C, and carefully agitated (for a maximum of 20 s) as the mixture melted to ensure homogeneity. Subsequently, the heated mixture remained unstirred. Aliquots were taken at prescribed times by removing a drop of solution with a fresh glass pipet, and immediately dispersing it into EtOH (25 mL). The EtOH dispersion was divided into two 16 $\times$ 100 mm test tubes using additional EtOH to fill the tubes, which were centrifuged for two minutes (benchtop centrifuge). The EtOH was decanted and hexane (5 mL) was added to redisperse the nanocrystals. Specimens were prepared for TEM analysis as described below. TEM analysis was completed within 24 h of the preparation of the hexane dispersions.

The collection of aliquots continued for 140−300 min, depending on the TOABr concentration employed. Reliable kinetic data were obtained up to the initial signs of sedimentation, which indicated gross aggregation or bulk-gold precipitation.

Preparation of TEM Samples. The hexane dispersions of nanocrystals were further diluted with an additional 2−3 mL of hexane, achieving a light pink color, to ensure a light nanocrystal coverage on the TEM grids upon deposition. One to two drops were pipetted onto a grid in air and evaporated to dryness at room temperature. All sample grids were analyzed by TEM within one hour of preparation to preclude nanocrystal ripening on the grid prior to analysis. No evidence of nanocrystal growth or agglomeration was observed during TEM analysis.

Measurement of Nanocrystal Sizes and Size Distributions. Digital TEM images were obtained from several locations on the sample grid. The normal bright field images were saved in a TIF format and resampled using image-processing software to increase the resolution to 400 dpi. The particle diameter distributions were measured from multiple images using Image-Pro Express software (www.mediacy.com). A minimum of 400−1000 particles were measured for each sample, and all particles in a given image were measured to obtain an accurate ratio of small to large nanocrystals. This practice was particularly important for bimodal early time distributions, as these samples required larger numbers of particles to be measured overall to ensure accuracy. Periodically, 2000 or more particles were measured to compare the mean, standard deviation, and shape of the distribution to corresponding values obtained from smaller counts. No significant difference was detected on these occasions, indicating that the number of particles measured was sufficient to produce reliable statistics.

Results

Determination of the Nucleation Function. In this study, we obtained nucleation functions comparable in shape to those of Wette and co-workers[46] in Figure 2. Following

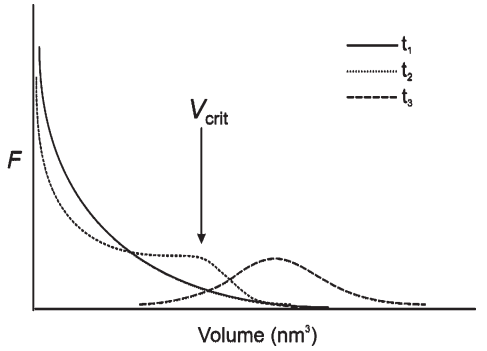

Figure 3. Schematic diagram of the characteristic time evolution of the CSD in particle growth. CSDs are plotted as the fraction of nanoparticles of a given volume (F) vs nanoparticle volume. Volume refers to the volume of individual nanoparticles. The time points t_1, t_2, and t_3 refer to starting, early, and later times, respectively. The CSDs are shown to evolve from asymptotic at t_1, to bimodal at t_2, and to unimodal at t_3 (and later times).

the suggestion of Gualtieri[59] we show that Gaussian fits to these curves (Figure 2) provide reasonable approximations of their shapes. Because our nucleation-rate data were extracted from CSDs determined from TEM images, they are less extensive than Wette's.[46] Consequently, we employed Gaussian approximations rather than extensively determined nucleation functions in this work.

Studies of particle growth, including by aggregative processes, have established that the CSDs follow a characteristic time evolution, as diagrammed in Figure 3,[22−24,30,41,42,60−63] with a peak emerging at the critical size. Initially, the CSD typically has an asymptotic shape. Subsequently, a peak emerges in the early time CSDs,[30,41,60−63] which then shifts to progressively larger size. The emergence of the peak results from a burst of nucleation,[42] as the nucleation rate increases rapidly.[41] In aggregative growth, this event is the formation of critical aggregates, which is an aggregative-nucleation process. Consequently, the peak first appears at the critical-aggregate size.[42] Knowledge of the critical-aggregate size allows extraction of the nucleation function from the early time CSDs, as described below.

In this study, the conditions for the thermal coarsening of thiolate-capped Au nanocrystals closely approximated those reported in the original studies by Zhong and coworkers.[1,2] The kinetics were determined as a function of TOABr concentration (see the Experimental Section). The starting nanocrystals, prepared by the Brust synthesis,[3] had a mean diameter of 1.68 nm with a standard deviation in the diameter distribution of 0.36 nm, as determined by TEM (Figure 4a). Hereafter, these initially prepared Au nanocrystals are referred to as primary nanocrystals.

For each kinetic trial, CSDs were measured by TEM at time intervals. In these trials, the aggregated Au nanocrystals readily coalesced, such that roughly spherical nanoparticles, rather than tight aggregates of nanoparticles,

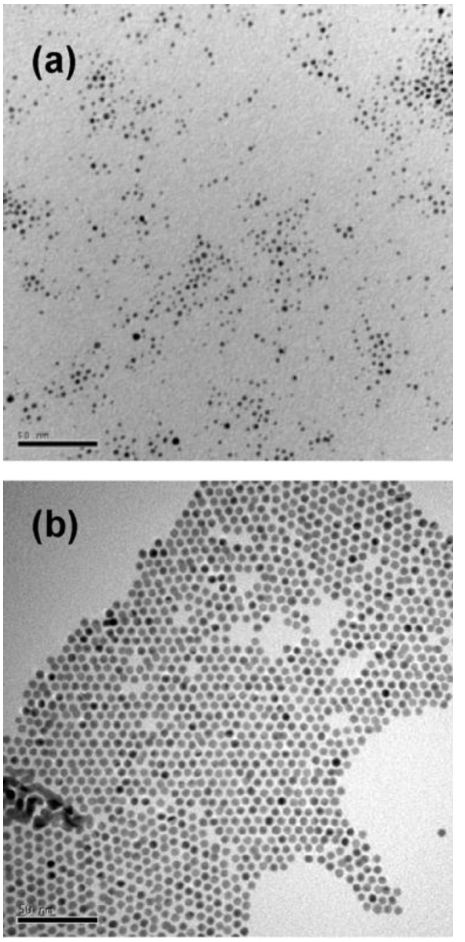

Figure 4. Representative TEM images of decanethiolate-capped Au nanocrystals. The quantity following the ± symbol is one standard deviation in the diameter distribution, expressed as a percentage of the mean diameter. (a) Primary nanocrystals having a mean diameter d = 1.68 nm ± 21%; (b) nanocrystals thermally coarsened with [TOABr] = 0.362 M, having a mean diameter d = 5.37 nm ± 7.1%.

dominated the TEM images (Figure 4b). Some aggregates of primary nanoparticles were found. More significantly, polycrystalline nanoparticles were imaged by HRTEM at early times, prior to their coalescence into single nanocrystals (see below).

Diameter distributions were measured from the TEM images and converted to volume distributions by assuming spherical morphologies. The volume data so obtained were binned using the minimum bin width that avoided excessive noise or discontinuities in the resulting CSDs. A constant bin width was used to construct the early time CSDs, through the emergence of a peak at the critical volume. Figure 5 plots the early time CSDs from one such trial with a TOABr concentration of 0.145 M. A peak first emerged (30 min) at a nanoparticle volume of 21 ± 3 nm^3 (bin width = 6 nm^3), which is the volume of the critical aggregate, V_{crit}. This critical volume corresponds to 8.5 ± 1.3 mean primary nanocrystals. The V_{crit} values so measured were not highly sensitive to bin width; the values determined over a range of bin widths were within the experimental error. The CSDs in Figure 5 may be compared to the idealized CSDs in Figure 3. The CSDs and V_{crit} values for the other kinetics trials are

(59) Gualtieri, A. F. *Phys. Chem. Minerals* **2001**, *28*, 719–728.
(60) Gusak, A. M.; Hodaj, F.; Bogatyrev, A. O. *J. Phys.: Condens. Matter* **2001**, *13*, 2767–2787.
(61) Talukdar, S. S.; Swihart, M. T. *J. Aerosol Sci.* **2004**, *35*, 889–908.
(62) Lümmen, N.; Kraska, T. *J. Aerosol Sci.* **2005**, *36*, 1409–1426.
(63) Mukherjee, D.; Prakash, A.; Zachariah, M. R. *J. Aerosol Sci.* **2006**, *37*, 1388–1399.

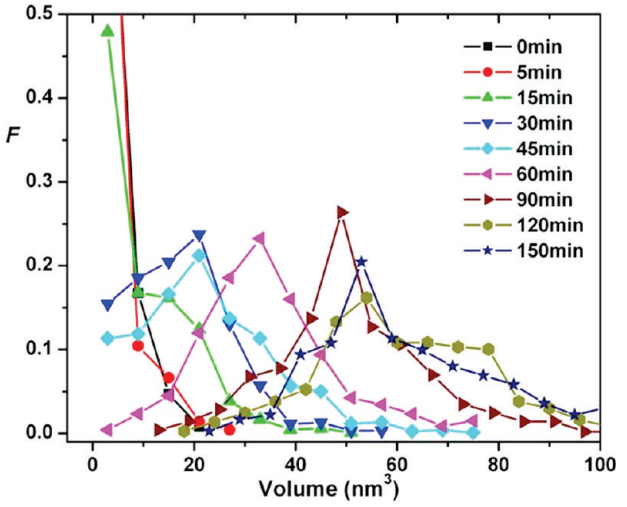

Figure 5. CSDs for the coarsening trial conducted with [TOABr] = 0.145 M, at the times indicated in the inset legend. The data were binned using a bin size of 6 nm^3 for all CSDs. A peak is evident at V_{crit} = 21 nm^3 in the CSDs at 30 and 45 min. CSDs are plotted as the fraction of nanoparticles of a given volume (F) vs nanoparticle volume. Volume refers to the volume of individual nanoparticles.

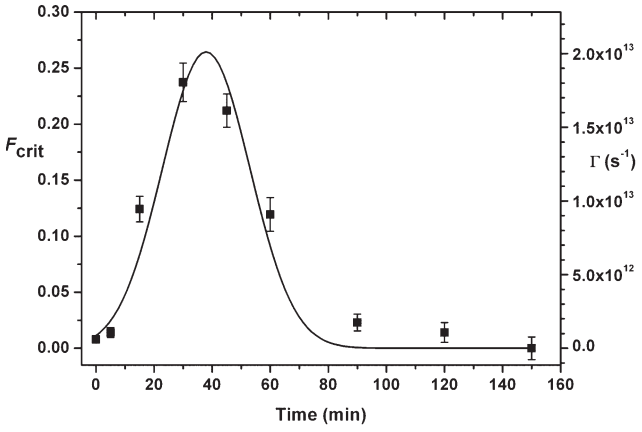

Figure 6. Nucleation function and Gaussian fit for the coarsening trial conducted with [TOABr] = 0.145 M. The left and right axes correspond to the critical-aggregate fraction F_{crit} and the scaled nucleation rate Γ, respectively (see text).

in Supporting Information Figures S3−S8 and Table S2, respectively.

The proportion of aggregates in the CSD having the critical size or volume rises and falls with the aggregative-nucleation rate, Γ.[46,62] Consequently, the fraction F_{crit} of the aggregates in the CSD having the critical volume V_{crit} is proportional to Γ, and hence the time dependence of F_{crit} is proportional to the nucleation function, Γ vs t. Therefore, F_{crit} was determined for each CSD as the nanoparticle count inside the bin containing V_{crit} divided by the total nanoparticle count. The results extracted from the CSDs in Figure 5 are plotted as a function of time in Figure 6, along with a Gaussian fit to the data. Figure 6 constitutes an experimental curve that is proportional to the nucleation function for this trial ([TOABr] = 0.145 M).

The maximum aggregative nucleation rate Γ_{max} was determined and the nucleation function (Figure 6) scaled as $\Gamma(t)$ by the following procedure. The total number N of aggregative nuclei formed was calculated by dividing the total volume of Au used by the final mean nanocrystal volume (Table 1). The height h of a Gaussian curve is related to its area A and width 2σ according to eq 1. For the nucleation function, the area is equal to N, the width to Δt_n (the 2σ breadth of the time window for nucleation), and the height to Γ_{max} (eq 2). In this case $N = (4.57 \pm 0.51) \times 10^{16}$ and $\Gamma_{max} = (2.01 \pm 0.24) \times 10^{13}$ s^{-1}. (The reader will note that Γ_{max} and $\Gamma(t)$ in general are *rates* not rate *constants*; they report the number of critical aggregates formed per second at a given time, within the *entire* experiment. Because the *number* of critical aggregates is unitless, the units on Γ_{max} and $\Gamma(t)$ are s^{-1}.) Accordingly, the function was rescaled by the right-hand vertical axis in Figure 6.

$$h = \frac{A}{2\sigma\sqrt{\pi/2}} \quad (1)$$

$$\Gamma_{max} = \frac{N}{\Delta t_n \sqrt{\pi/2}} \quad (2)$$

Nucleation functions were similarly obtained for the kinetics over a range of TOABr concentrations, and the results are plotted in Figure 7. (Individual plots of each trial including error bars are provided as Supporting Information Figures S9−S14.) Figure 7 and Table 1 reveal that as the TOABr concentration was increased the width of the time window for nucleation Δt_n first decreased from 30 ± 1 min and then remained at about 12 ± 1 min upon reaching a minimum for [TOABr] ≥ 0.446 M. As the TOABr concentration was increased, the nucleation function also progressively shifted to shorter times. This shift is quantified by τ_n, the time at which Γ_{max} was achieved. Table 1 shows that τ_n varied from 38 ± 1 min at low [TOABr] to 8 ± 1 min at high [TOABr]. Therefore, increasing TOABr concentration increased the rates of and decreased the time period for aggregative nucleation.

Interestingly, in most of the trials the maximum aggregative-nucleation rate Γ_{max} remained fairly constant near $(2.0 \pm 0.2) \times 10^{13}$ s^{-1}. Only the trial at [TOABr] = 0.362 M deviated slightly from this pattern, having a $\Gamma_{max} = (2.6 \pm 0.4) \times 10^{13}$ s^{-1}. However, even this apparent difference was small and within the error of the measurement (see Figure 8). Even so, the pattern observed here (Figure 7) differed considerably from that reported by Wette[46] (Figure 2), for which the shift of the nucleation function to shorter time and narrower widths was accompanied by a significant, progressive increase in Γ_{max}.

Fitting the Nanocrystal Growth Kinetics. The size-vs-time plots for nanocrystal growth typically exhibit sigmoidal profiles like that in Figure 1.[15−19,35,64−66] The initial induction-like period is associated with nucleation, which is the formation of critical aggregates in the case of

(64) Talapin, D. V.; Rogach, A. L.; Haase, M.; Weller, H. *J. Phys. Chem. B* **2001**, *105*, 12278–12285.
(65) Hiramatsu, H.; Osterloh, F. E. *Chem. Mater.* **2004**, *16*, 2509–2511.
(66) Skrdla, P. J.; Robertson, R. T. *Chem. Mater.* **2008**, *20*, 3–4.

Table 1. Aggregative Nucleation and Growth Parameters Extracted from the Kinetic Data for Au-Nanoparticle Coarsening As a Function of TOABr Concentration

[TOABr] (M)	τ_n (min)[a]	Δt_n (min)[b]	N ($\times 10^{16}$)[c]	Γ_{max} ($\times 10^{13}$ s^{-1})[d]	k_g ($\times 10^{-2}$ s^{-1})[e]	n[f]
0.145	37.93 ± 0.86	30.19 ± 1.15	4.56 ± 0.51	2.01 ± 0.24	1.44 ± 0.079	2.011 ± 0.333
0.264	34.78 ± 0.87	29.53 ± 1.63	4.31 ± 0.47	1.94 ± 0.24	1.72 ± 0.093	2.333 ± 0.381
0.362	20.92 ± 0.29	17.79 ± 1.11	3.47 ± 0.37	2.59 ± 0.44	2.21 ± 0.107	1.775 ± 0.238
0.446	19.06 ± 0.29	12.31 ± 0.59	1.81 ± 0.17	1.96 ± 0.21	2.53 ± 0.056	2.664 ± 0.156
0.579	16.62 ± 0.31	13.7 ± 0.56	2.19 ± 0.21	2.13 ± 0.23	3.15 ± 0.101	2.070 ± 0.176
0.634	14.10 ± 0.41	12.4 ± 0.90	1.89 ± 0.18	2.03 ± 0.24	2.88 ± 0.186	2.107 ± 0.349
0.681	7.85 ± 0.64	11.14 ± 1.35	1.80 ± 0.17	2.15 ± 0.33	1.71 ± 0.111	1.354 ± 0.136

[a] Time taken for maximum nucleation rate to be achieved. [b] Time window for nucleation. [c] Total number of critical aggregates. [d] Maximum nucleation rate. [e] Growth rate. [f] Avrami exponent.

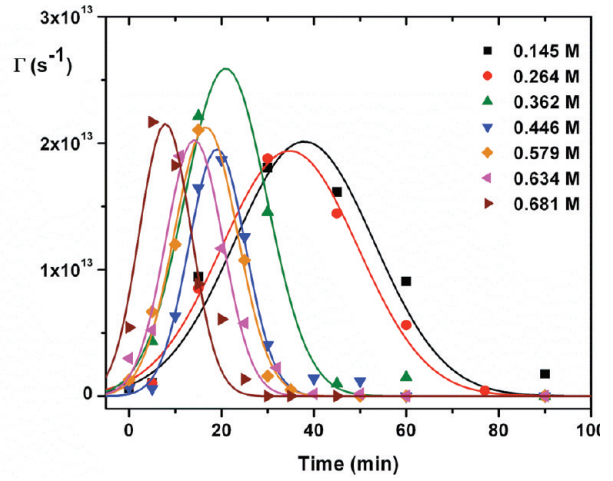

Figure 7. Nucleation functions for the kinetic trials conducted at various TOABr concentrations. The individual [TOABr] values are given in the inset legend.

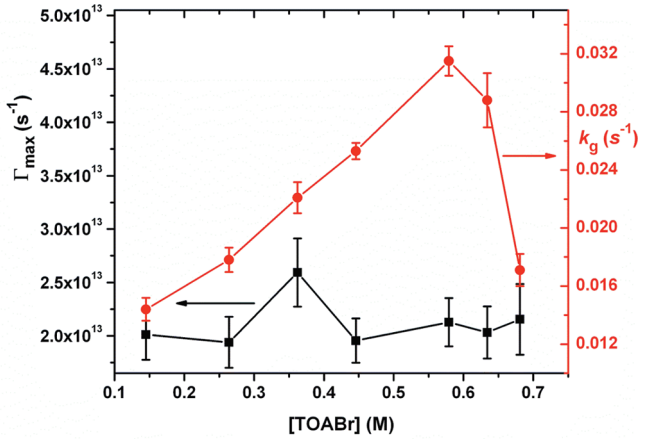

Figure 8. Plots of the maximum nucleation rate Γ_{max} (black squares, left axis) and growth rate k_g (red circles, right axis) vs TOABr concentration.

aggregative growth. The nucleation regime is followed by an active growth regime in which supercritical nanocrystals, derived from the critical aggregates, grow by aggregation with primary nanocrystals, until the primary nanocrystals are consumed. Ostwald ripening may occur at the conclusion of active growth under appropriate conditions. We did not observe Ostwald ripening in our experiments until later times, beyond the end of our kinetic trials.

The growth profiles as presented in plots of nanocrystal mean volume $\bar{V}$ vs time were sigmoidal. The $\bar{V}(t)$ data

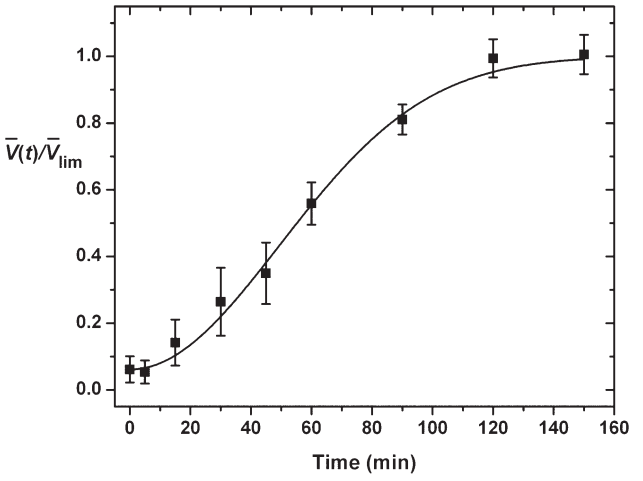

Figure 9. Kinetic data and the eq 3 fit for the trial conducted at [TOABr] = 0.145 M. $\bar{V}(t)$ is the nanocrystal mean volume at a specific time, and $\bar{V}_{lim}$ is the final nanocrystal mean volume.

were extracted from the nanocrystal-volume distributions determined at time intervals, as described above, and scaled by the final mean nanocrystal size $\bar{V}_{lim}$. Thus, nanocrystal growth was followed by plotting $\bar{V}(t)/\bar{V}_{lim}$ vs t. The growth kinetics so obtained were fit to a KJMA equation[67−70] (eq 3) having two fitting parameters, a growth-rate parameter k_g and an Avrami exponent n. The parameter $\bar{V}_i$ is the primary nanocrystal mean volume. Kinetic data collected at a TOABr concentration of 0.145 M and the resulting fitted curve are plotted in Figure 9.

$$\frac{\bar{V}(t)}{\bar{V}_{lim}} = \frac{\bar{V}_i}{\bar{V}_{lim}} + \left(1 - \frac{\bar{V}_i}{\bar{V}_{lim}}\right)(1 - \exp(-k_g t)^n) \qquad (3)$$

All sets of kinetic data collected as a function of TOABr concentration are plotted in Figure 10, with their eq-3 fits. (The individual plots with error bars are Figures S15−S20 in the Supporting Information.) The fitted k_g and n values are recorded in Table 1, and the k_g values are also plotted in Figure 8. Although the *quality* of the fits was sensitive to the value of the Avrami exponent n, the fitted *values* of k_g were insensitive to this parameter over n = 1−3

(67) Avrami, M. *J. Chem. Phys.* **1939**, *7*, 1103–1112.
(68) Avrami, M. *J. Chem. Phys.* **1940**, *8*, 212–224.
(69) Avrami, M. *J. Chem. Phys.* **1941**, *9*, 177–184.
(70) Burbelko, A. A.; Fraś, E.; Kapturkiewicz, W. *Mater. Sci. Eng., A* **2005**, *413−414*, 429–434.

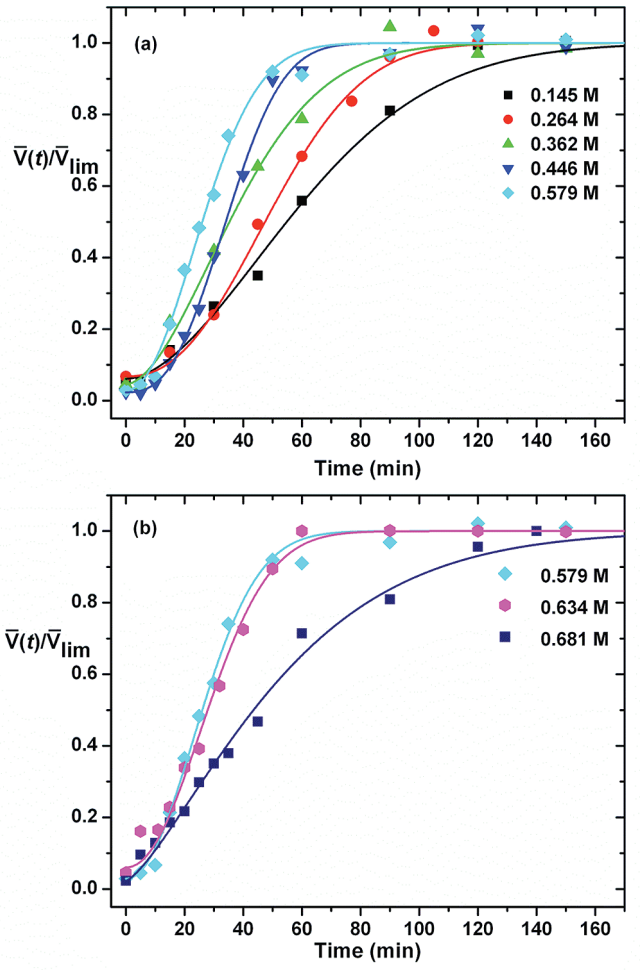

Figure 10. Kinetic data and the eq-3 fits for trials conducted at various TOABr concentrations. The individual [TOABr] values are given in the inset legends. (a) 0.145−0.579 M; (b) 0.579−0.681 M.

(see Supporting Information Table S3), the typical range for the Avrami exponent.[71] Thus, we considered the k_g values to be a robust indicator of the *relative* growth rates.

In principle, the k parameters extracted from KJMA analyses convolve nucleation and growth rates.[70,72] However, we will show in the Discussion that k_g here is strongly associated with growth rates, and imperceptibly or only weakly to nucleation rates. The results reveal that the growth rates first increased, passed through a maximum, and then decreased with increasing [TOABr]. The minimum and maximum k_g values differed by only an approximate factor of 2 (Table 1).

Evidence for Aggregative Nucleation and Growth. We have argued here for a nonclassical process in which nucleation proceeds by formation of a critical aggregate of primary nanocrystals. Growth then proceeds by the subsequent addition of primary nanocrystals to the critical and supercritical aggregates. One must also consider if growth proceeds instead by an Ostwald-ripening mechanism in which primary particles dissolve and are reprecipitated onto larger nanocrystals, presumably the larger of the primary nanocrystals in the initial CSD.

Therefore, we used TEM and high-resolution TEM (HRTEM) to distinguish between an aggregative-growth and Ostwald-ripening processes. In the former case, nucleation and growth should *initially* produce primary-nanocrystal aggregates, and then polycrystalline nanoparticles, with their constituent domains derived from the primary nanocrystals. In the latter case, the growing nanoparticles should be single nanocrystals, because they would have grown from deposition of molecular nutrients onto single-crystal primary nanoparticles.

We did find small aggregates of primary nanocrystals in the early time TEM images of coarsening trials (Supporting Information Figure S21). However, these aggregates may have formed on the TEM grid rather than under coarsening conditions. A dominant characteristic of the early time images was the coexistence of small numbers of distinctly larger nanoparticles with the abundant primary nanocrystals (Supporting Information Figure S22), suggesting that nanocrystal coalescence followed rapidly after primary-nanocrystal aggregate formation. Consequently, we determined the internal texture of the larger, supercritical nanoparticles as described below.

Figure 11 contains HRTEM images of Au nanoparticles after approximately 10 min under coarsening conditions. The images reveal polycrystalline domain structures, wherein the number and mean size of the domains are consistent with the mean primary nanocrystal. For example, the nanoparticle in Figure 11a has a diameter of 4 nm, and a mean domain size of 1.5 nm, which compares favorably to the mean primary nanocrystal size of 1.7 nm. An aggregated nanoparticle having a diameter of 4 nm should consist of 13 primary-nanocrystal-derived domains, 8 of which are discernible in Figure 11a. The remainder is likely obscured by overlap, especially near the center of the nanoparticle image where the depth trajectory is the longest.

Only a fraction of the early time nanoparticles exhibited polycrystalline structures; the rest were single crystals. Although we did not examine a statistically significant number of nanoparticles in the HRTEM study, we estimate that 20−40% were polycrystalline. We surmised that the remaining nanoparticles had already undergone coalescence to single crystals within the 10 min growth period. Thus, we propose that *all* of the nanoparticles were initially polycrystalline.

HRTEM images of the nanoparticles after 60 min of coarsening established that at least 95% were single crystals. A small fraction ($\leq$5%) exhibited multiply twinned structures[73−75] (see Supporting Information Figure S23). The multiply twinned structures likely evolved from the initial polycrystalline architectures as suggested by Turkevich[28] and Uyeda,[43] because they are

(71) Christian, J. W. *The Theory of Transformation in Metals and Alloys*, 2nd ed.; Pergamon: Oxford U.K., 1981; p 489.
(72) Levine, L. E.; Narayan, K. L.; Kelton, K. F. *J. Mater. Res.* **1997**, *12*, 124–132.
(73) Ino, S. *J. Phys. Soc. Jpn.* **1969**, *27*, 941–953.
(74) Wiley, B.; Sun, Y.; Chen, J.; Cang, H.; Li, Z.-Y.; Li, X.; Xia, Y. *MRS Bull.* **2005**, *30*, 356–361.
(75) Sato, K.; Huang, W. J.; Bohra, F.; Sivaramakrishnan, S.; Tedjasaputra, A. P.; Zuo, J. M. *Phys. Rev. B* **2007**, *76*, 144113.

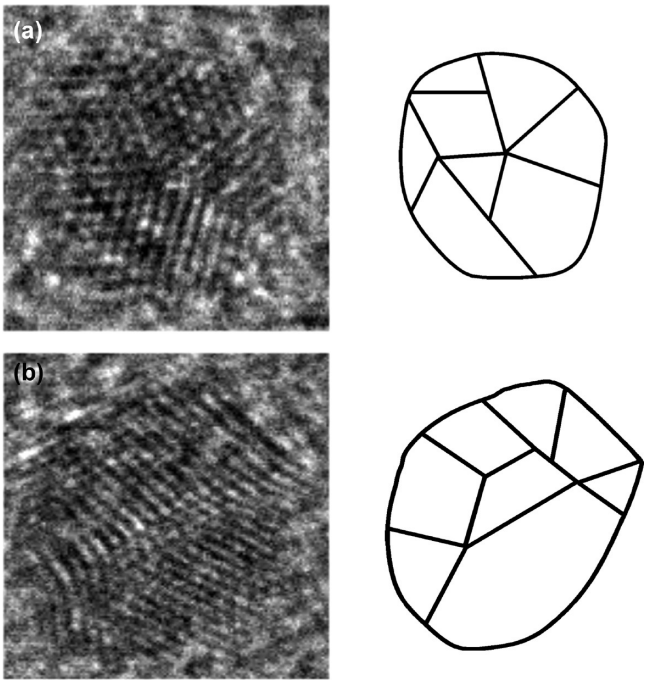

Figure 11. High-resolution TEM images of polycrystalline Au nanoparticles obtained after coarsening for ~10 min. The line drawings depict the crystalline domains that can be discerned in the images.

unlikely to have developed later within initially single-crystal nanoparticles.[73−75] The results suggested that over time most or all of the initially polycrystalline nanoparticles coalesced to single crystals. The HRTEM results are therefore most consistent with aggregative growth. If growth was by Ostwald ripening, none of the early time nanoparticles should have possessed polycrystalline structures.

Further evidence of aggregative nucleation and growth was the observation of bimodal CSDs at intermediate stages of coarsening. Figure 12 is a representative TEM image taken from a kinetics run a few minutes after τ_n, the time at which Γ_{max} was achieved. The image clearly shows a population of small, primary nanocrystals, and a second population of much larger nanoparticles, with few nanoparticles of intermediate size. The CSD corresponding to Figure 12 is provided in Supporting Information Figure S24. Aggregative processes are known to produce such bimodal distributions,[13,61,76−84] because aggregation introduces a second population of particles that are distinctly larger than the primary particles.[13,78]

In contrast, Ostwald ripening generally proceeds by a unimodal, self-similar CSD that broadens and shifts with

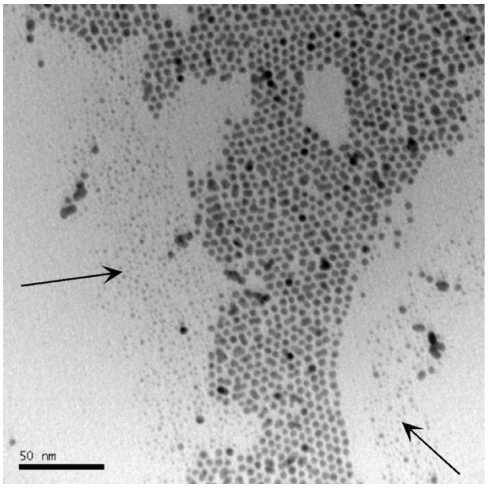

Figure 12. TEM image from a coarsening trial at an intermediate time showing a bimodal distribution of coarsened and primary nanocrystals. Note that the coarsened (center) and primary (left and right) nanocrystals are largely segregated into separate regions of the TEM grid. The primary-nanocrystal regions are identified by arrows. The scale bar is 50 nm.

time, but does not bifurcate.[64,84−88] The generation of a bimodal distribution by Ostwald ripening requires special circumstances, specifically, a mass-exchange-rate discontinuity at a critical nanocrystal size.[89] As described in the Discussion, one origin of such a rate discontinuity is a nanocrystal-morphology change occurring at a specific size. Such a special circumstance does not exist here. The bimodality we observed resulted from the emergence and evolution of the peak at the critical-aggregate size V_{crit} in the CSDs (see Figure 5), which coexisted with the primary nanocrystals until they were all consumed by aggregative growth.

Finally, the sigmoidal growth kinetics we observed (Figure 10) are inconsistent with the LSW model for equilibrium Ostwald ripening, which asserts a linear growth in nanoparticle volume $\bar{V}$ vs time.[90,91] As noted above, we did observe Ostwald ripening to occur after very long times, considerably beyond the conclusion of our kinetic trials (Supporting Information Figure S25). Additionally, we observed Ostwald ripening to occur in TEM specimens that had been allowed to stand for several hours before analysis. However, the combined results of nanoparticle structure, the evolution of the CSDs, and the growth kinetics argue strongly against Ostwald ripening as the dominant growth mechanism during the active-growth period.

Discussion

Use of a KJMA Expression to Assess Growth Rates. KJMA or Avrami models, such as eq 3, are rigorously applicable to the kinetics of certain solid-state phase transformations.[70−72] However, KJMA analyses have

(76) Halfon, A.; Kaliaguine, S. *Can. J. Chem. Eng.* **1976**, *54*, 168–172.
(77) Budz, J.; Jones, A. G.; Mullin, J. W. *J. Chem. Technol. Biotechnol.* **1986**, *4*, 153–161.
(78) Beckman, J. R.; Farmer, R. W. *AIChE Symp. Ser.* **1987**, *83*, 85–94.
(79) Xiong, Y.; Pratsinis, S. E. *J. Aerosol Sci.* **1991**, *22*, 637–655.
(80) Hostomský, J.; Jones, A. G. *J. Phys. D: Appl. Phys.* **1991**, *24*, 165–170.
(81) Wachi, S.; Jones, A. G. *Chem. Eng. Sci.* **1992**, *47*, 3145–3148.
(82) Eberl, D. D.; Drits, V. A.; Środon, J. *Am. J. Sci.* **1998**, *298*, 499–533.
(83) Park, K. S.; Lee, B. W.; Choi, M. *Aerosol Sci. Technol.* **1999**, *31*, 258–274.
(84) Carlow, G. R. *Phys. A* **1997**, *239*, 65–77.
(85) Mantzaris, N. V. *Chem. Eng. Sci.* **2005**, *60*, 4749–4770.
(86) Madras, G.; McCoy, B. J. *J. Colloid Interface Sci.* **2003**, *261*, 423–433.
(87) Datye, A. K.; Xu, Q.; Kharas, K. C.; McCarty, J. M. *Catal. Today* **2006**, *111*, 59–67.
(88) Vorhees, P. W. *Annu. Rev. Mater. Sci.* **1992**, *22*, 197–215.
(89) Zheng, X. *Z. Phys. B* **1994**, *93*, 501–507.
(90) Lifshitz, I. M.; Slyozov, V. V. *J. Phys. Chem. Solids* **1961**, *19*, 35–50.
(91) Wagner, C. *Z. Elektrochem.* **1961**, *65*, 581–590.

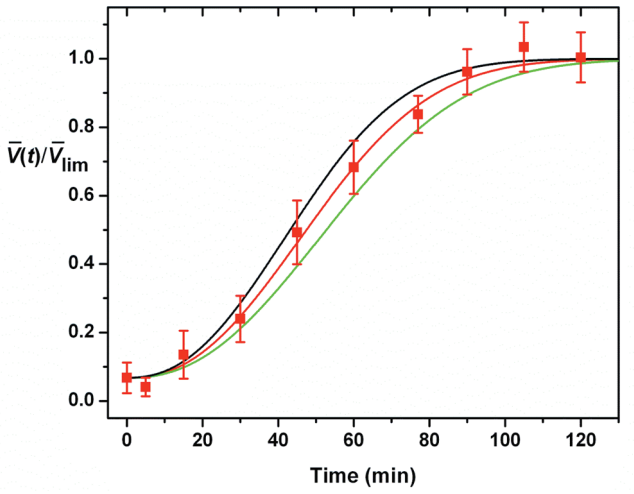

Figure 13. Kinetic data (red squares) from Figure 9, and the eq 3 fit (red curve) using the optimized values of k_g and n. Equation 3 fits are also provided in which k_g has been increased (black curve) and decreased (green curve) by 10% from the optimized value (while n is held at its optimized value). These curves show that k_g functions primarily as a fitting parameter for the rapidly rising, active-growth regime in the kinetic data.

also been applied to solution-based or melt crystallization of zeolites,[92] lipids,[93−95] polymers,[96,97] β-hemeatin,[98] and colloidal crystals,[46] and to nanocrystal growth.[66] As in eq 3, KJMA expressions generally contain two kinetic parameters: an Avrami exponent n, the value of which is often related to the nucleation mechanism and dimensionality of growth, and a rate parameter k that convolves nucleation and growth rates. Although the rates of nucleation and growth are not separately parametrized, we show below that our k_g (eq 3) is most strongly dependent on growth behavior and is thus a reliable indicator of *relative* growth rates.

Figure 13 plots a set of kinetic data ([TOABr] = 0.264 M) and the eq 3 fit using the optimized values for k_g and n. Two additional curves are plotted, one in which k_g has been increased by 10% from the optimal value, and one in which k_g has been decreased by 10% (both at the original optimized n). The reader will note that the fits to the initial induction period, associated with nucleation, are scarcely affected by the variations in the k_g value. However, the fits in the rising portion of the sigmoidal data, the active growth regime, are strongly affected. The k_g values at $\pm$10% of the optimal value provide considerably poorer fits to the growth-regime data. We therefore conclude that k_g is much more strongly reflective of growth rates than of nucleation rates.

Although attractive in its simplicity, the KJMA analysis used here (eq 3) is incomplete, as it follows only the growth of the mean nanoparticle size and not the evolution of the entire CSD. As shown here (Figure 3) and elsewhere,[22−24,30,41,42,60−64,82] CSDs evolve in time according to mechanistically informative patterns, and complete kinetic studies of nanocrystal growth should explicitly address them. Distributed-kinetics approaches follow the kinetic fate of every size in a time-evolving CSD by assuming a mechanism, encoding the size dependences of the kinetic parameters into population-balance equations, and simulating or fitting the CSDs as a function of time.[22−26,30,31,41,42,61,63,66,85,97,99] However, such approaches are computationally intensive and so are neither convenient nor generally accessible to the nanocrystal-synthesis community.

We use the simple analytical expression in eq 3 only to obtain relative quantitative comparisons of growth rates as a function of TOABr concentration. We note that the same information can be assessed qualitatively merely by visual inspection of the slopes of the rising portions of the kinetic plots in Figure 10. Other analytical models also exist for fitting nanoparticle-growth data,[65,66] one of which will be investigated in a subsequent paper.[47] Furthermore, not all nanocrystal-growth data can be fit by a KJMA expression or other analytical models.[100] Therefore, the relative growth rates extracted with eq 3 are used below in only a careful, limited manner.

Exclusion of Ostwald Ripening as the Origin of the Observed Bimodal CSDs. As noted above, theoretical studies indicate that Ostwald ripening is generally incapable of producing a bimodal size distribution,[84,88] unless a discontinuity exists in interparticle-exchange rates.[89] Studies of particle-coarsening on surfaces have found that such rate discontinuities can be generated by particle-shape changes, such as between domed and faceted morphologies, occurring at a critical size.[101−104] Bimodal size distributions result, as one morphology ripens faster than the other. Similar observations have been made for nanocrystals ripened under hydrothermal conditions.[105] A rate discontinuity induced by substrate-particle strain has also been proposed as the origin of bimodal CSDs developed by Ostwald ripening.[106] However, there is no substrate-particle strain or distinct morphology changes in our Au-nanocrystal ripening experiments, ruling out Ostwald ripening as the origin of the early time bimodal CSDs.

Theoretical[107] and experimental[108,109] studies also show that bimodal distributions initially formed by various

(92) Norby, P. *J. Am. Chem. Soc.* **1997**, *119*, 5215–5221.
(93) Price, F. P.; Wendorff, J. H. *J. Phys. Chem.* **1971**, *75*, 2839–49.
(94) Yang, C. P.; Nagle, J. F. *Phys. Rev. A* **1988**, *37*, 3993–4000.
(95) van Osdol, W. W.; Ye, Q.; Johnson, M. L.; Biltonen, R. L. *Biophys. J.* **1992**, *63*, 1011–1017.
(96) Di Lorenzo, M. L.; Silvestre, C. *Prog. Polym. Sci.* **1999**, *24*, 917–950.
(97) Yang, J.; McCoy, B. J.; Madras, G. *J. Chem. Phys.* **2005**, *122*, 064901.
(98) Egan, T. J.; Tshivhase, M. G. *Dalton Trans.* **2006**, 5024–5032.
(99) Rempel, J. Y.; Bawendi, M. G.; Jensen, K. F. *J. Am. Chem. Soc.* **2009**, *131*, 4479–4489.
(100) Finney, E. E.; Finke, R. G. *Chem. Mater.* **2009**, *21*, 4468–4479.
(101) Vine, D. J.; Jesson, D. E.; Morgan, M. J.; Shchukin, V. A.; Bimberg, D. Phys. Rev. B **2005**, *72*, 241304(R).
(102) Ross, F. M.; Tersoff, J.; Tromp, R. M. *Microscopy Microanal.* **1998**, *4*, 254–263.
(103) Agnelli, M.; Kolb, M.; Mirodatos, C. *J. Catal.* **1994**, *148*, 9–21.
(104) Takaki, T.; Tomita, Y. *Key Eng. Mater.* **2007**, *340−341*, 1073–1078.
(105) Wahi, R. K.; Liu, Y.; Falkner, J. C.; Colvin, V. L. *J. Colloid Interface Sci.* **2006**, *302*, 530–536.
(106) Goldfarb, I.; Hayden, P. T.; Owen, J. H. G.; Briggs, G. A. D. *Phys. Rev. B* **1997**, *56*, 10459–10468.
(107) Chen, M. K.; Voorhees, P. W. *Modell. Simul. Mater. Sci. Eng.* **1993**, *1*, 591–612.
(108) Ryu, H. J.; Hong, S. H.; Weber, J.; Tundermann, J. H. *J. Mater. Sci.* **1999**, *34*, 329–336.
(109) Howard, A.; Mitchell, C. E. J.; Egdell, R. G. *Surf. Sci. Lett.* **2002**, *515*, L504–L508.

means can be *accentuated* by Ostwald ripening. That is, the smaller mode shrinks in particle size and number as the larger mode increases in particle size and number. The initial bimodal CSDs can be generated by successive nutrient dosing,[109] by successive heat treatments at different temperatures,[110] by secondary nucleation processes,[111] or simply by combining two unimodal populations.[107] In such cases, Ostwald ripening is not the *origin* of the bimodal distributions, but does *increase* the separation between the two modes.

Despite the theoretical findings against it,[64,84−89] experimental observations of bimodal size distributions generated in coarsening studies on surfaces are occasionally attributed to Ostwald ripening, or proposed as evidence of it.[106,109,112−115] Indeed, it is tempting to imagine that smaller particles shrinking and larger particles growing could generate a bifurcation and thus bimodality in an initially unimodal CSD. However such claims are not supported theoretically. Except under the special circumstances noted above,[89,101−105] the shrinking and growing particles remain within a single, evolving, self-similar, unimodal CSD.

We contend that the observations of bimodal distributions attributed to Ostwald ripening result instead from the alternative origins described above. In one case, strain appears to have generated a rate discontinuity.[106] In other cases, bimodal distributions are initially present.[109,112] In other cases, Ostwald ripening has been assumed,[113] evidence for aggregation and coalescence has been ignored,[114] or aggregation and coalescence has not been compellingly excluded.[115] Therefore the *generation* of a bimodal CSD may be properly attributed to aggregative growth, but not to Ostwald ripening.

Kinetic Evidence for the Electrostatic Stabilization of Thiolate-Capped Au Nanocrystals. Thiolate-capped Au nanocrystals are sterically stabilized; that is, solvent dispersions of nanocrystals are stable against flocculation because of steric interactions between the ligand monolayer coatings on adjacent nanocrystals.[116] However, Schiffrin and co-workers demonstrated that Au nanocrystals prepared by the two-phase Brust synthesis,[3] employed here for the primary nanocrystals, retain significant amounts of TOABr, a synthetic phase-transfer agent.[4] They proposed an electric double-layer-like structure (Figure 3 in ref 4) with bromide ions bound to the nanocrystal surface interspersed with the thiolates, and with a second, outer shell of *n*-octyl$_4$N$^+$ counterions

Scheme 1. Schematic Depiction of the Collapse of the Electric Double Layer about the Au Nanocrystals with a Sufficient Amount of Added TOABr[a]

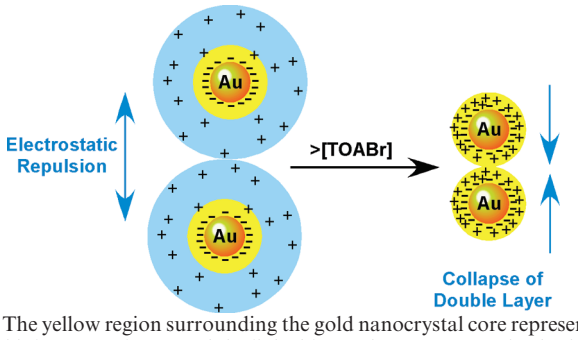

[a] The yellow region surrounding the gold nanocrystal core represents the thiolate monolayer, and the light-blue region represents the double-layer (the extent of the octyl$_4$N$^+$counterion atmosphere). The octyl$_4$N$^+$ ions are depicted by plus signs, and the Br$^-$ ions attached to the Au surfaces by minus signs. At low ionic strength (left) the octyl$_4$N$^+$counterion atmosphere is extended due to mutual octyl$_4$N$^+$ ion repulsions. The extended octyl$_4$N$^+$counterion atmospheres on adjacent nanoparticles repel one another, preventing the close approach of nanoparticles, and thus inhibiting their aggregation. At high ionic strength (right) the double layer collapses due to screening, and the counterion atmosphere about each nanoparticle shrinks dramatically, allowing the close approach of nanoparticles. Only the steric barrier resulting from the thiolate monolayers remains to provide (a lesser) stabilization against aggregation.

(Scheme 1, left side). Schiffrin and co-workers used this structure to rationalize the low solubility of the Au-nanocrystal material retaining TOABr relative to that from which the TOABr had been exhaustively removed. They argued that the electric double-layer-like structure resulting from TOABr retention produced electrostatic interactions that increased the lattice energy (stabilization) of the solid, and thereby decreased its solubility (dispersibility).[4]

We are now extending this electrostatic-stabilization model[4] to account for the behavior of the thiolate-capped Au nanocrystals in solvent dispersion. These nanocrystals exhibited excellent dispersibility in the solvent system we employed. Standard DLVO theory asserts that such nanocrystals would also be electrostatically stabilized in *dispersion*, against aggregation and coalescence, by interparticle repulsions between the octyl$_4$N$^+$ outer shells (counterion "atmospheres" on adjacent nanocrystals, Scheme 1).[117] However, the degree of such electrostatic stabilization is dependent on the ionic strength of the medium (Scheme 1). We present kinetic evidence from the nucleation functions (Figure 7) in support of this proposal.

As noted in the Results, increasing TOABr concentrations caused the nucleation functions to progressively narrow and shift to earlier times (as quantified by Δt_n and τ_n, respectively, in Table 1). The results showed that added TOABr accelerated the aggregative-nucleation process. The narrowing of the nucleation function was dramatic at the lower TOABr concentrations, and then achieved a near-constant minimum of $\Delta t_n \approx 12$ min at higher TOABr concentrations. We interpret this behavior to indicate a collapse of the electric double layer at a

(110) Mrotzek, M.; Nembach, E. *Acta Mater.* **2008**, *56*, 150–154.
(111) Proussevich, A. A.; Sahagian, D. L.; Carlson, W. D. *J. Volcanol. Geotherm. Res.* **2007**, *164*, 112–126.
(112) Mitchell, C. E. J.; Howard, A.; Carney, M.; Egdell, R. G. *Surf. Sci.* **2001**, *490*, 196–210.
(113) Lai, X., St.; Clair, T. P.; Goodman, D. W. *Faraday Discuss.* **1999**, *114*, 279–284.
(114) LaLonde, A. D.; Norton, M. G.; Zhang, D.; Gangadean, D.; Alkhateeb, A.; Padmanabhan, R. *J. Mater. Res.* **2005**, *20*, 3021–3027.
(115) Kielbassa, S.; Häbich, A.; Schnaidt, J.; Bansmann, J.; Weigl, F.; Boyen, H.-G.; Ziemann, P.; Behm, R. J. *Langmuir* **2006**, *22*, 7873–7880.
(116) Templeton, A. C.; Hostetler, M. J.; Kraft, C. J.; Murray, R. W. *J. Am. Chem. Soc.* **1998**, *120*, 1906–1911.
(117) Hiemenz, P. C.; Rajagopalan, R. *Principles of Colloid and Surface Chemstry*, 3rd ed.; Marcel Dekker: New York, 1997; pp 585−604.

sufficient TOABr concentration, removing the electrostatic barrier for aggregative nucleation.

DLVO theory establishes that the Debye length, the thickness of the counterion atmosphere (electric double layer), depends on the ionic strength of the medium (Scheme 1).[117] At low ionic strength the counterion atmosphere is diffuse due to mutual electrostatic repulsions between the counterions (here, octyl$_4$N$^+$ ions), preventing close approach of adjacent particles. At higher ionic strength the counterion atmosphere shrinks and eventually collapses because the mutual repulsions are screened, and the electrostatic barrier to particle aggregation is thus removed.[22,24,118] At this point, the remaining barrier to aggregation (and thus nucleation) is the steric barrier presented by the intact thiolate monolayer on each nanoparticle.

We propose that the TOABr-derived electric double layer about the primary Au nanocrystals collapses completely at [TOABr] = 0.446 M (Table 1, Figure 7), resulting in the minimization of Δt_n. The narrowing of the nucleation function is rationalized by prior studies of reaction-limited vs diffusion-limited aggregation (RLCA and DLCA, respectively).[85,119] The "pure" RLCA and DLCA mechanisms form the limits of a spectrum of intermediate mechanisms, with the broadest final particle-size distribution generally obtained at the RLCA limit, and the narrowest at the DLCA limit.[85,119] The narrowest final particle-size distribution argues for the narrowest nucleation function. In the present case, a steric barrier due to the thiolate monolayer remains, and so the DLCA limit is approached at higher TOABr concentrations but is presumably not achieved.

Because the electrostatic barrier disappears at [TOABr] = 0.446 M, further narrowing of the nucleation function is not achieved at even higher TOABr concentrations. We speculate that the continued decrease in τ_n is a secondary ionic-strength effect on the remaining steric barrier. The observed dependence of the nucleation kinetics on TOABr concentration constitutes strong evidence of the (partial) electrostatic stabilization of thiolate-capped Au nanocrystals.[4]

Nucleation Control of the Final Nanocrystal Size and Size Distribution. As noted above, the narrowest nucleation function, parametrized by Δt_n, should correlate with the narrowest final CSD (that obtained at the end of the active-growth period). Figure 14 plots the relative standard deviation in the final CSD vs [TOABr], which shows a minimum near [TOABr] = 0.446 M, the lowest concentration at which the nucleation function obtained a near-constant minimum Δt_n. The minimum relative standard deviation of 0.057 (or 5.7% of the final mean nanocrystal size) is very close to the minimum value predicted theoretically for the liquid-phase synthesis of nanoparticles (7.1%).[85] At TOABr concentrations above 0.579 M, the final CSDs broaden, although the nucleation

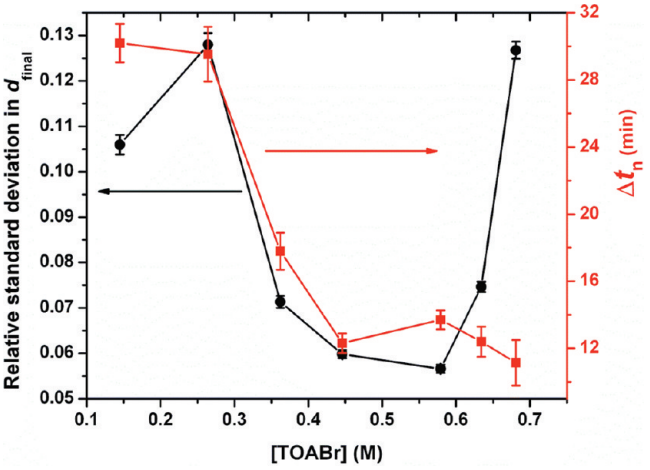

Figure 14. Plots of the relative standard deviation in the final nanocrystal diameter distribution (black circles, left axis) and the time window for nucleation Δt_n (red squares, right axis) vs TOABr concentration. The relative standard deviation is the standard deviation in the diameter divided by the final mean nanocrystal diameter.

functions do not (Figure 14). We attribute this broadening to the significant solvent viscosity increases at high TOABr concentrations.[120] The results strongly suggest that nucleation control of the *width* of the final size distribution was achieved.

We argued above that the final nanocrystal mean size should be determined by the total amount of Au present and N, the number of critical aggregates formed, which is the area under the nucleation function. Equation 2 establishes that the width (Δt_n) and height (Γ_{max}) of the nucleation function are equally influential in determining N. However, in the present work the minimum and maximum values of Δt_n varied by a factor of 3, whereas the minimum and maximum values of Γ_{max} varied by only a factor of 1.29 and were within experimental error of one another (Figure 8). Consequently, we would expect the final nanocrystal mean size to also correlate most strongly here with Δt_n, as does the width of the final CSD (see above).

The near-constant Γ_{max} values contrast with those reported by Wette and co-workers[46] (Figure 2), in which the narrowing and shifting of the nucleation function to earlier times were accompanied by progressive increases in Γ_{max}. Although the time-dependent nucleation rates generally increased here with TOABr concentration, as indicated by the progressively decreasing τ_n values, Γ_{max} did not systematically increase (Figures 7 and 8 and Table 1), as in Figure 2. However, Wette and co-workers achieved increases in Γ_{max} by increasing the initial primary-particle volume fraction, which was only incidentally varied over a small range in our study. We also note that two opposing influences operate on Γ_{max}: the rate at which the critical aggregates are formed, and the rate at which they are consumed by growth (k_g). Figure 8 shows that k_g increased steadily with increasing TOABr concentration, until the highest concentrations, at which the viscosity increased dramatically. We surmise that the increasing

(118) Van Hyning, D. L.; Klemperer, W. G.; Zukoski, C. F. *Langmuir* **2001**, *17*, 3120–3127.
(119) Anderson, V. J.; Lekkerkerker, H. N. W. *Nature* **2002**, *416*, 811–815.
(120) Abdullin, S. N.; Stepanov, A. L.; Osin, Yu. N.; Khaibullin, R. I.; Khaibullin, I. B. *Surf. Coat. Technol.* **1998**, *106*, 214–219.

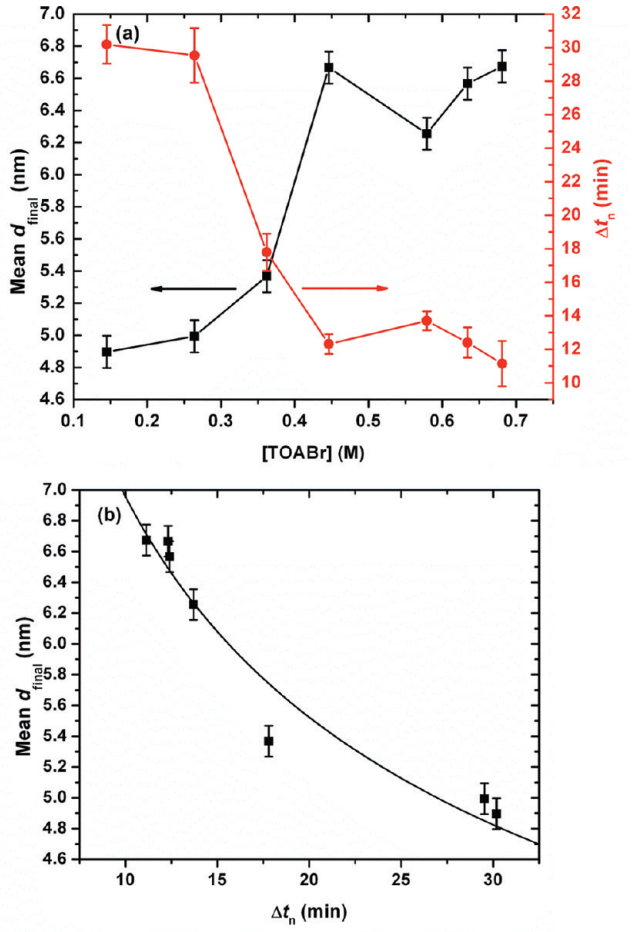

Figure 15. (a) Plots of the final nanocrystal mean diameter (black squares, left axis) and Δt_n (red circles, right axis) vs TOABr concentration. (b) Plot of the final nanocrystal mean diameter vs Δt_n. The curve is the theoretical dependence of the mean d_{final} on Δt_n assuming a constant, averaged value for Γ_{max} (see text).

growth rates constrained Γ_{max} to the observed near-constant values. As a result N, and thus the final nanocrystal mean size, should correlate with Δt_n.

As Δt_n decreases N also decreases, and the final nanocrystal mean size should increase, as a constant amount of Au is divided among fewer nanocrystals. This expectation is confirmed in Figure 15a, which plots the final nanocrystal mean size and Δt_n vs [TOABr]. Remarkably, the two curves are nearly mirror images of one another, indicating a strong correlation of final size and Δt_n.

This strong correlation is further evidenced in Figure 15b, which plots the final nanocrystal mean size vs Δt_n. The curve in Figure 15b is the theoretical dependence of the final mean diameter on Δt_n assuming a constant value for Γ_{max} (see the Supporting Information for the derivation of this function). The assumed value is the average of the Γ_{max} values in Table 1. The agreement between the data and curve establish convincingly that the final nanocrystal mean size is controlled primarily by the width of the nucleation function. The combined results confirm that both the width of the final CSD and the final mean size were under nucleation control.

Unfortunately, the final nanocrystal size was varied over only a small range in this study, 4.9−6.7 nm, which is not synthetically useful. To gain synthetic utility, N would be purposefully varied over a much larger range. Ideally, one would maintain a minimized Δt_n by using an optimal amount of salt or other nucleation-control additive, to ensure an optimally narrow final CSD. Therefore, N would ideally be controlled by variations of Γ_{max}, which thus becomes the preferred size-control parameter.

As revealed by the results above, we have not yet determined how to purposefully vary Γ_{max}. However, Γ_{max} has been shown to increase systematically with increasing primary-particle volume fraction[46] (Figure 2) or nutrient concentration.[28] In an analogous field, the rate of formation of gas-phase clusters is a power-law function of pressure, P^{α} with $1 < \alpha < 3$.[121−123] Thus, the nucleation of gas-phase clusters increases rapidly with pressure. We expect to find a similar relationship between Γ_{max} and primary-particle volume fraction or nutrient concentration, providing directions for further research.

Conclusions

As noted above, we were initially motivated to pursue these studies by the reports of Zhong and co-workers that small, thiolate-capped Au nanocrystals having broad initial CSDs could be ripened, in the presence of the coarsening agent TOABr, to larger nanocrystals having narrow CSDs.[1,2] We were surprised by these results because they seemed inconsistent with standard Ostwald ripening, the mechanism we assumed to be operative. However, Zhong and co-workers suggested an aggregative-growth mechanism, which we now confirm by the results herein.

The primary evidence against Ostwald ripening was the observation of bimodal size distributions at early times, polycrystalline particles, and sigmoidal growth kinetics, as detailed above. However, Ostwald ripening is not a nucleation-driven process. If nanoparticle growth occurred by Ostwald ripening here, then there would have been no critical size and no nucleation function. In that event we could not have observed the strong correlation between the final nanoparticle mean size and size distribution with Δt_n, which is shown in Figures 14 and 15.

Schiffrin and co-workers first reported that thiolate-capped Au nanocrystals persistently retain TOABr and proposed an electric-double-layer-like structure.[4] Here, we found that the aggregative growth of thiolate-capped Au nanocrystals is largely governed by the electric-double-layer stabilization of the nanocrystals. Addition of TOABr collapses the electric double layer, increasing the rates of aggregative nucleation and sharpening the aggregative-nucleation function. Because the maximum nucleation rate Γ_{max} is insensitive to the TOABr concentration, the width of the nucleation function Δt_n controls both the final size and size distribution of the ripened nanocrystals.

(121) Buck, U. *J. Phys. Chem.* **1988**, *92*, 1023–1031.
(122) Yasuoka, K.; Zeng, X. C. *J. Chem. Phys.* **2007**, *126*, 124320.
(123) Goldstein, N.; Brack, T. L.; Atkinson, G. H. *J. Chem. Phys.* **1986**, *85*, 2684–2691.

This work demonstrates that gaining control over the nucleation function (Γ_{max} and Δt_n) is the key to achieving rational synthetic control of nanocrystal mean sizes and the minimization of size distributions. In this study we achieved systematic control over the width of the nucleation function (Δt_n), but not its height (Γ_{max}). Ideally, nanocrystal size distributions will be minimized by minimizing Δt_n, and nanocrystal sizes will be manipulated by purposeful variations in Γ_{max}. Thus, important synthetic advances in nanocrystal synthesis will be possible when Γ_{max} can be systematically controlled.

Finally, the results suggest the great synthetic potential of aggregative growth. One may potentially vary aggregative-nucleation rates, and therefore the nucleation function, by varying any factor that influences nanocrystal stability, including the use of salts and other additives, the presence of stabilizing agents such as ligands and polymers, and variations in precursor or primary-particle concentrations, solvents, and temperature. Nucleation rates in *classical* nucleation and growth are not as predictably manipulated, and the corresponding nucleation functions cannot presently be experimentally determined. Thus, aggregative growth should allow means of synthetic control that are not otherwise available.

Acknowledgment. We thank Profs. Richard G. Finke (Colorado State U.), Lev D. Gelb (Washington U.), K. F. Kelton (Washington U.), Richard A. Loomis (Washington U.), Guy Genin (Washington U.), and Mr. Patricio La Rosa (Washington U.) for helpful discussions. We also thank Dr. Patrick Wette (German Aerospace Center, Bonn) for approving our use of Figure 2. We are grateful to the National Science Foundation for funding this work under grant no. CHE-0518427.

Supporting Information Available: Tables of the dependence of k_g on n and V_{crit} as a function of [TOABr]; plots of a primary-particle CSD, the dependence of total volume on the mass of TOABr used, CSDs for several coarsening trials, nucleation functions with error bars for several coarsening trials, and the kinetic data with error bars and eq 3 fits for several coarsening trials; an HRTEM image of a multiply twinned nanoparticle, and the derivation of the function plotted in Figure 15b. This material is available free of charge via the Internet at http://pubs.acs.org.